Materials Horizons

ROYAL SOCIETY OF CHEMISTRY

COMMUNICATION

View Article Online
View Journal | View Issue

Cite this: *Mater. Horiz.*, 2026, 13, 1005

Received 3rd September 2025,
Accepted 14th October 2025

DOI: 10.1039/d5mh01679g

rsc.li/materials-horizons

Self-healing redox chemistry in Cu–TiO_2 photocatalysts for enhanced hydrogen production

Mariyum Yousaf,[a] Hui Hu,[a] Faheem Abbas,[c] Xuxing Chen,[a] Yongge Wei,[c] Muhammad Sohail*[b] and Yun Gao*[a]

Hydrogen production from sunlight and abundant feedstock is central to a sustainable energy future, yet most efficient photocatalysts rely on costly noble metals. Here we report a scalable one-pot synthesis of CuO_x–TiO_2 photocatalysts that achieve a methanol-assisted hydrogen evolution rate of 30.6 mmol g^{-1} h^{-1}, among the highest reported for Cu-based systems. The optimized 12% CuO_x–TiO_2 maintains >90% activity retention over 50 h and performs reproducibly at the gram scale, underscoring its industrial potential. Spectroscopic and computational analyses uncover a dynamic CuO ⇆ Cu_2O ⇆ Cu^0 cycle and a previously unrecognized corrosion–healing redox loop, in which transient $Cu(OH)_2$ is continuously reduced back to Cu_2O by methanol-derived intermediates. This self-healing mechanism stabilizes the active Cu_2O phase, suppresses deactivation, and sustains long-term performance. Density functional theory reveals near-optimal hydrogen adsorption free energy (ΔG_{H^*} = −0.06 eV) on Cu–TiO_2(101), comparable to Pt(111), confirming copper's potential as a low-cost alternative to noble metals. These findings establish redox self-healing catalysis as a powerful design principle for durable, scalable, and earth-abundant photocatalysts for solar hydrogen production.

New concepts

This work introduces a simple one-pot synthesis of CuO_x–TiO_2 photocatalysts with precise control over Cu^0, Cu^+, and Cu^{2+} redox states. Beyond achieving a record methanol-assisted hydrogen evolution rate (>30 mmol g^{-1} h^{-1}) with excellent stability and scalability, we reveal a novel corrosion–healing redox loop at the CuO_x–TiO_2 interface. In this process, transient $Cu(OH)_2$ formed under illumination is dynamically reduced back to Cu_2O by methanol-derived intermediates, sustaining the active Cu_2O phase and preventing irreversible deactivation. This self-healing cycle, coupled with an S-scheme charge transfer pathway, provides a new mechanistic design principle for robust and scalable photocatalysts, bridging fundamental redox chemistry with real-world hydrogen production technologies.

1. Introduction

The transition to clean and renewable energy systems has placed hydrogen (H_2) at the forefront as a promising energy carrier due to its high energy density and carbon-free combustion.[1–5] However, current hydrogen production is dominated by methanol steam reforming (MSR), which is energy-intensive (for example, 200–350 °C and 20–50 bar), carbon-emitting, and of high cost.[6–8] Photocatalytic reforming of methanol–water mixtures offers an attractive alternative for solar-to-fuel (STF) conversion: methanol contains 12.5 wt% hydrogen and water contains 11.1 wt% hydrogen, and their combination enables hydrogen release under ambient conditions with lower thermodynamic barriers than for water splitting alone.[9–19] However, the deployment of photocatalytic hydrogen evolution remains constrained by the reliance on noble-metal cocatalysts such as Pt, Ru, or Rh, whose scarcity and cost limit scalability. Replacing these with earth-abundant metals requires not only high activity but also a fundamental understanding of how dopant chemistry governs interfacial charge transfer, stability, and durability under operating conditions.[20–31]

Among earth-abundant candidates (Ni, Fe, Zn, and Co), copper-doped TiO_2 (Cu–TiO_2) is particularly promising due to the multiple accessible oxidation states (Cu^0, Cu^+, and Cu^{2+}), which can act as electron mediators, hole scavengers, or active sites depending on the local environment.[23,26,32,33] Under illumination, these oxidation states coexist dynamically at CuO_x–TiO_2 interfaces, generating heterojunctions that promote charge separation and oxygen vacancy (Ov) formation.[8,34–44]

[a] *Ministry of Education Key Laboratory for the Green Preparation and Application of Functional Materials, School of Materials Science & Engineering, Hubei University, Wuhan, Hubei 430062, People's Republic of China. E-mail: gaoyun@hubu.edu.cn*

[b] *Department of Natural Sciences, Faculty of Science and Engineering, Manchester Metropolitan University, Manchester M15 6BX, UK. E-mail: muhammad.sohail@mmu.ac.uk*

[c] *Department of chemistry, Key lab of organic optoelectronics and Molecular Engineering of Ministry of Education, Tsinghua University, Beijing, 100084, P. R. China*

Such a dynamic system leads to an ambiguous relationship among microscopic structure, active sites, and catalytic performance.[18,45,46] Previous approaches, including single-atom Cu doping (CuSAs–TiO_2), ternary heterostructures (Cu/TiO_2/$SrTiO_3$), and rare-earth co-doping (Pr-CuSA–TiO_2), have shown performance improvements but suffer from complex synthesis, poor reproducibility, and limited scalability.[36,42,47–57]

Despite considerable research, several key challenges remain unresolved: the upper limit of stable Cu incorporation in TiO_2, the precise location of Cu species in the lattice *versus* surface, and the role of reversible Cu redox cycling in sustaining long-term activity. Excessive doping often leads to agglomeration of metallic Cu, collapse of mesoporosity, and accelerated recombination, while under-doping fails to exploit the redox flexibility of Cu.[55,58] The mechanistic understanding also remains elusive: while Cu_2O is frequently suggested as the active hydrogen evolution site, the competing contributions of CuO and Cu^0, and their interplay with surface hydroxyl groups (OH^-) and oxygen vacancies (Ov), are not clearly established.[23,38,49,59–64] Consequently, there is a critical need for a synthetic strategy that can precisely tune Cu^0/Cu^+/Cu^{2+} ratios and simultaneously reveal how their interconversion influences catalytic performance and durability.

Here, we report a scalable one-pot hydrothermal synthesis of CuO_x–TiO_2 photocatalysts that directly addresses these challenges. By regulating Cu incorporation, we achieve a balanced synergy of Cu redox states at an optimal loading of 12 wt%, yielding a record methanol-assisted hydrogen evolution rate of 30.6 mmol g^{-1} h^{-1}, nearly an order of magnitude higher than that of pristine TiO_2.[65] Through *operando* spectroscopic analysis, we uncover a previously unrecognized corrosion–healing redox loop, in which transient $Cu(OH)_2$ formed during illumination is dynamically reduced back to Cu_2O by methanol-derived intermediates (Fig. 7).[39] This self-healing cycle stabilizes Cu_2O active sites, suppresses irreversible deactivation, and underpins the long-term durability of the catalyst.[39] Together with an S-scheme heterojunction charge-transfer pathway, where metallic Cu acts as an electron sink, and DFT confirmation of near-Pt hydrogen adsorption energetics ($\Delta G_{H^*} \approx -0.06$ eV on Cu–TiO_2(101)), our results establish not only the scalability of Cu-based photocatalysts but also introduce redox self-healing catalysis as a new design principle for durable, earth-abundant hydrogen evolution systems.[38]

2. Results and discussion

2.1. Scalable one-pot synthesis enables precise control of Cu redox states

Developing Cu-based photocatalysts that are both active and scalable requires synthetic control over the interplay of Cu^0, Cu^+, and Cu^{2+} species, which govern charge separation and interfacial dynamics. Conventional multi-step or post-treatment strategies often suffer from poor reproducibility, phase segregation, and uncontrolled reduction, leading to inconsistent catalytic performance.[22,66,67] To overcome these limitations, we designed a one-pot hydrothermal route in which $Ti(OBu)_4$ and $Cu(NO_3)_2$ precursors undergo co-condensation in the presence of HF, enabling direct incorporation of Cu species into the TiO_2 lattice (Fig. 1). This method not only preserves the anatase phase up to 14 wt% Cu loading but also stabilizes a balanced mixture of CuO, Cu_2O, and metallic Cu at the catalyst surface.

The optimized 12% Cu–TiO_2 material exhibits a record HER rate of 30.6 mmol g^{-1} h^{-1} in methanol photo reforming (MPR), an order of magnitude higher than pristine TiO_2. Importantly, the synthesis was reproduced at the gram scale (6 g per batch) with a negligible variation in performance, establishing scalability and reproducibility that are rarely demonstrated in Cu–TiO_2 systems. Beyond activity, this material displays exceptional durability, maintaining >90% of its HER performance over 50 h of continuous operation, a stability that correlates with the dynamic restructuring of Cu redox states.[66]

Structural and spectroscopic analyses reveal that this synthetic approach enables a self-regulating CuO ⇆ Cu_2O ⇆ Cu^0 cycle, where excess Cu after the doping limit segregates into surface heterojunctions without collapsing the anatase lattice.

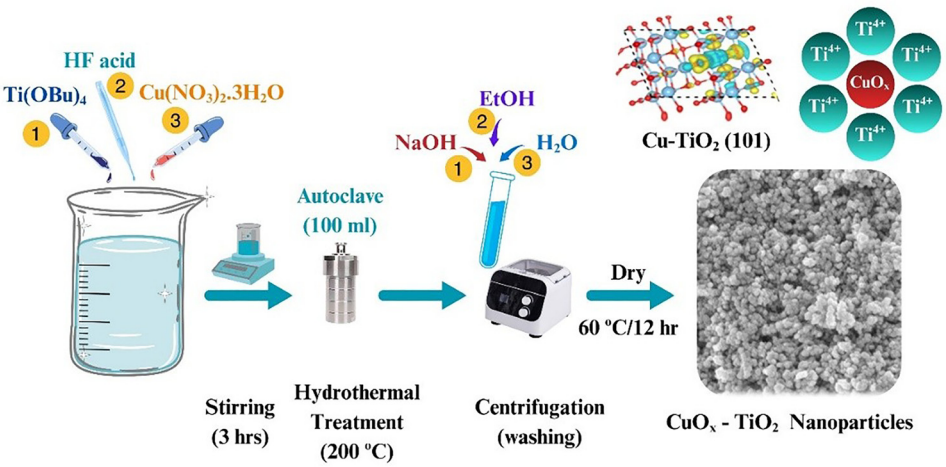

Fig. 1 Schematic illustration of the one-pot hydrothermal synthesis of the CuO_x–TiO_2 photocatalyst.

This dynamic redox interplay is central to both the enhanced hydrogen evolution and the prevention of irreversible Cu_2O oxidation. In particular, we identify a corrosion–healing redox loop, in which photogenerated holes oxidize Cu_2O to CuO/$Cu(OH)_2$, while methanol-derived intermediates subsequently reduce these back to Cu_2O, continuously regenerating the active phase.[39] This self-healing mechanism, revealed through *operando* XRD, XPS and supported by DFT, is a previously unrecognized pathway that explains the long-term stability of Cu–TiO_2 catalysts.

2.2. Structural and morphological stability of Cu doped TiO_2

Powder X-ray diffraction (XRD) and Raman spectra of pristine TiO_2 and CuO_x–TiO_2 with varying copper doping levels (1–14 wt%) confirmed the presence of a 100% photocatalytically active TiO_2(101) anatase phase (Fig. 2). Maintaining the anatase phase at such high Cu doping levels is attributed to the one-pot synthetic method, where an increase in % Cu doping leads to a broadening, intensity reduction and positive shifts for the prominent XRD peak Cu–TiO_2(101) at 2θ = 25.3° (Fig. 2b).[33,50] This suggests a high Cu^{2+} dispersion within the TiO_2 crystal lattice, leading to strong structural and optoelectronic modifications due to Cu–O–Ti bonds and the formation of oxygen vacancies (O_v).[68,69] However, beyond 10% Cu doping, characteristic metallic copper (Cu^0)(111) peak intensity begins to appear at 2θ = 43.3°, which increases with % Cu doping (Fig. 2a). For 12% Cu–TiO_2, additional peaks corresponding to oxidized Cu^+ (Cu_2O)(111) at 2θ = 36.0° and Cu^{2+} (CuO)(111) at 2θ = 35.2° were also observed (Fig. 2a, c and Fig. S3). Beyond 12%, metallic Cu is the dominating species which overshadows Cu_2O and CuO peaks in XRD. This suggests that after reaching the Cu doping limit, excess Cu starts depositing on the surface within the mesoporous TiO_2 pore channels, forming heterojunctions of multiple Cu oxidation states at CuO_x–TiO_2(101) interfaces.[70] The Cu doping threshold is likely influenced by the synthetic method and may vary with different synthesis parameters. Over 50 h of irradiation, the XRD spectra of 12% Cu–TiO_2 show significant growth of a strong, intense peak for Cu_2O at 2θ = 36.62° at the expense of CuO at 2θ = 35.2°, confirming the conversion of CuO into stable Cu_2O during the HER (Fig. 2c).

Consistent with XRD results, Raman vibrational modes at 142.7 cm^{-1} (E_g), 395 cm^{-1} (B_{1g}), 515.7 cm^{-1} (B_{2g}) and 636.36 cm^{-1} ($E_{g(3)}$) confirm the presence of a TiO_2 anatase phase (Fig. 2a).[65,71] With an increase in % Cu doping, the E_g peak intensity at 142.7 cm^{-1} significantly broadened and blue shifted by 3.5 cm^{-1} to a higher wave number of 146.11 cm^{-1}, confirming high Cu dispersion, abundance of oxygen vacancies (Ov), and structural defects in the TiO_2 crystal lattice (Fig. 2e).[72–74] This shift suggests lattice compression and a strong interaction between guest Cu^{2+} and host TiO_2 to facilitate fast electron transfer at the CuO_x–TiO_2 interface.[69,75–78] A progressive blue shift was also observed over 20 h of irradiation (Fig. S2). Contrary to a recent report, annealing up to 500 °C does not affect the anatase TiO_2 crystal phase (Fig. S3), highlighting its industrial relevance for developing photocatalytic sheets or panels for practical applications.[12,59,79]

The porous characteristics of Cu–TiO_2 and pristine TiO_2 were analyzed using Brunauer–Emmett–Teller (BET) measurements (Fig. S4a–f and Table S1). In comparison, the surface area of 83.9 $m^2\ g^{-1}$, the pore volume of 0.31 $cm^3\ g^{-1}$, and the average pore size of 14.7 nm have placed 12% Cu–TiO_2 in between 11% and 13% Cu–TiO_2 (Fig. S4a–c). This "sandwiched" behavior validates that once the Cu^{2+} doping limit is

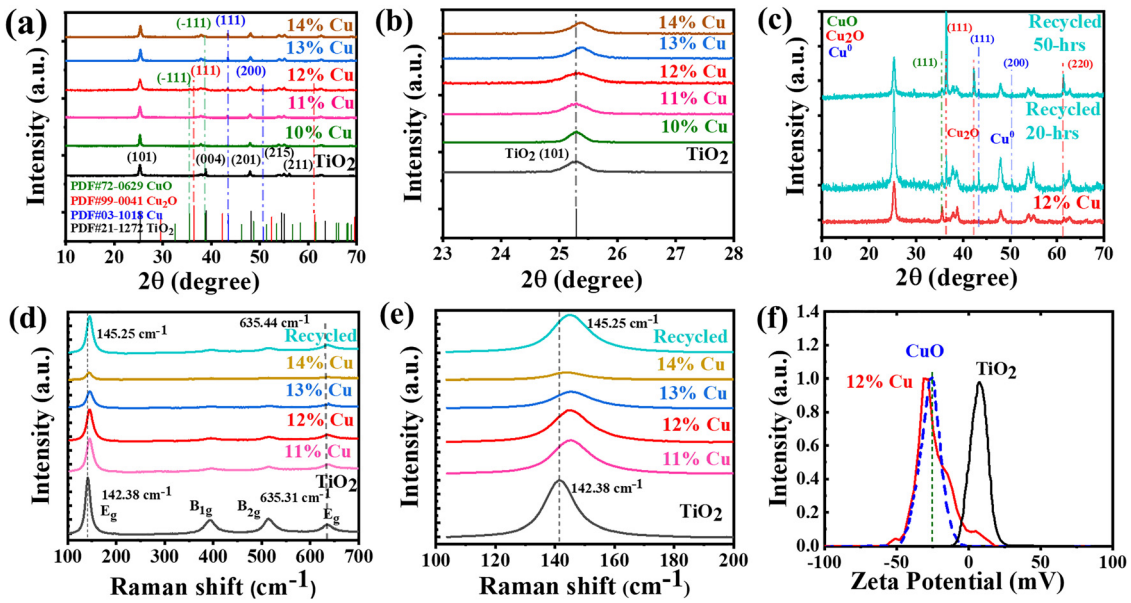

Fig. 2 (a) XRD patterns of the pristine TiO_2 and % Cu–TiO_2. (b) Partially magnified spectra. (c) XRD of the optimized 12% Cu–TiO_2 sample before and after 50 h of HER. (d) Raman spectroscopic analysis of pristine and % Cu–TiO_2 before and after 20 h of HER. (e) Partial magnified Raman spectra. (f) Surface charge measurement of pristine TiO_2, CuO & Cu–TiO_2 *via* zeta-potential.

reached, reduced Cu_2O and Cu^0 species begin to deposit, agglomerate, and form clusters at the surface, leading to pore clogging—a trend consistent with XRD results.[80,81] The N_2 adsorption isotherm follows a Type IV profile with an H3 hysteresis loop, indicating the presence of mesoporous structures.[82] Additionally, the Barrett–Joyner–Halenda (BJH) N_2 adsorption isotherm confirms the pore size distribution and the catalyst's porous nature (Fig. S4d–f). However, a slight variation in the surface area between 11%, 12%, and 13% Cu–TiO_2 indicates that the surface area alone may not be the primary factor responsible for the enhanced photocatalytic activity.

Furthermore, when the 12% Cu–TiO_2 catalyst is dispersed in water, hydration, protonation, and deprotonation processes lead to surface charging, causing the nanoparticles to behave like zwitterions. This is measured as a zeta potential, which depends on the suspension's isoelectric point (IEP).[83] Compared to the pristine TiO_2 (+3.4 mV at pH 5.09), 12% Cu–TiO_2 exhibits significantly negative zeta potential −28.9 mV, closely matching that of commercial CuO (−26.3 mV) (Fig. 2f). This supports the presence of a hydroxylated Cu layer (Cu–OH) at the surface, which enhances charge accumulation and transfer, thereby promoting hydrogen production.[84] The higher surface charge also prevents particle aggregation, improving stability in water. This stability is attributed to charge imbalance caused by the substitution of Ti^{4+} atoms with Cu^{2+} in the TiO_2 lattice.[71]

The morphology and chemical composition of the best-performing 12% Cu–TiO_2 and pristine TiO_2 were further analyzed using scanning electron microscopy (SEM) and energy-dispersive X-ray spectrometry (EDS) (Fig. S5–S7). The uniform morphology consists of spherical-shaped particles aggregated into lamellar, cluster-like structures with clear boundaries, with an average size of 41 nm (Fig. 3a). High-angle annular dark-field scanning transmission electron microscopy (HAADF-EDS) mapping confirms the uniform dispersion of CuO_x over TiO_2 (Fig. S7a–f). High-resolution transmission electron microscopy (HRTEM) analysis reveals lattice spacing values of 0.34 nm and 0.36 nm, corresponding to Cu(220) and anatase TiO_2(101), respectively, matching well with the corresponding diffraction results (Fig. 3c).[85–88] Line scan analysis further demonstrates the homogeneous distribution of CuO_x within the nanoparticles (Fig. 3b). The coexistence of Cu^{1+} with Cu^0 at TiO_2 crystal lattice interfaces cannot be ignored, which is consistent with XRD results, confirming the formation of CuO_x–TiO_2 heterostructures.

These results indicate that 12% CuO_x–TiO_2 doping comprises $Cu^{2+}/Cu^{+}/Cu^0$ species, forming multiple heterojunctions that contribute to the high photocatalytic HER rate.[89,90] Therefore, developing a synthetic strategy to control the ratio of Cu^0/Cu^{+}/Cu^{2+} redox species by adjusting % Cu doping is crucial for optimizing photocatalytic performance.[21,91]

2.3. Optical properties of the CuO_x–TiO_2 photocatalyst

UV-visible absorption spectroscopy (UV-Vis) reveals a redshift in the light absorption edge of CuO_x–TiO_2, shifting from 447 nm to the visible region at 554 nm. This corresponds to a bandgap reduction from 3.0 eV for anatase TiO_2 to 2.5 eV for 12% Cu–TiO_2, as calculated using the Kubelka–Munk function. (Fig. 4a, b, and Table S2). The enhanced absorption in the visible region arises from introduced intermediate energy levels (Cu 3d states) within the band gap, which reduces the effective band gap, allowing absorption of visible light (400–800 nm) (Fig. 4a).[65] Cu doping into TiO_2 induces crystal lattice distortion and introduces defect states, creating additional energy levels near the conduction band that facilitate charge transfer.[22,92] Photoluminescence (PL) spectra exhibit a significant reduction

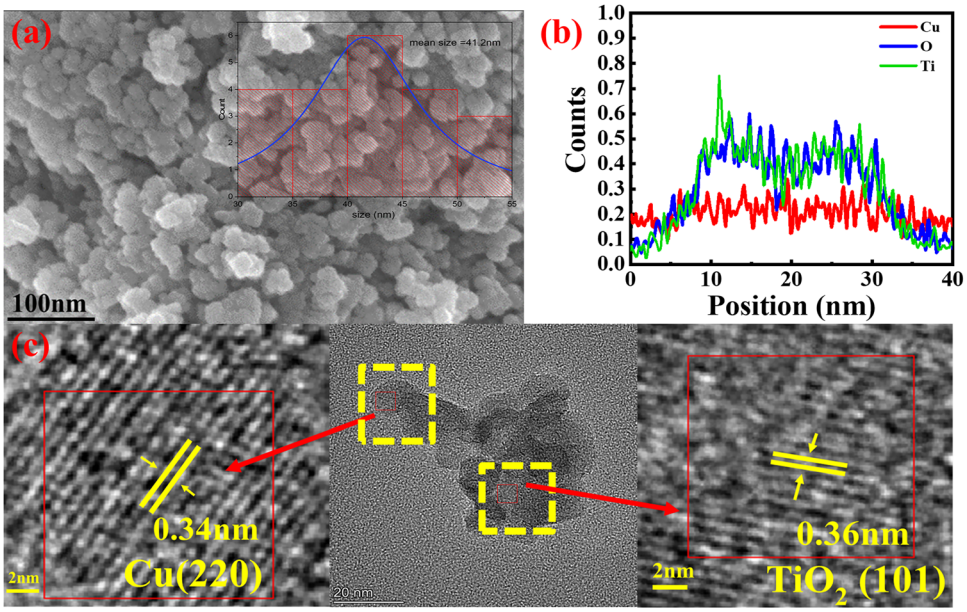

Fig. 3 Characterization images of 12% Cu–TiO_2. (a) SEM image. (b) EDS line scan of Cu, Ti, and O (c) HRTEM 12% Cu–TiO_2.

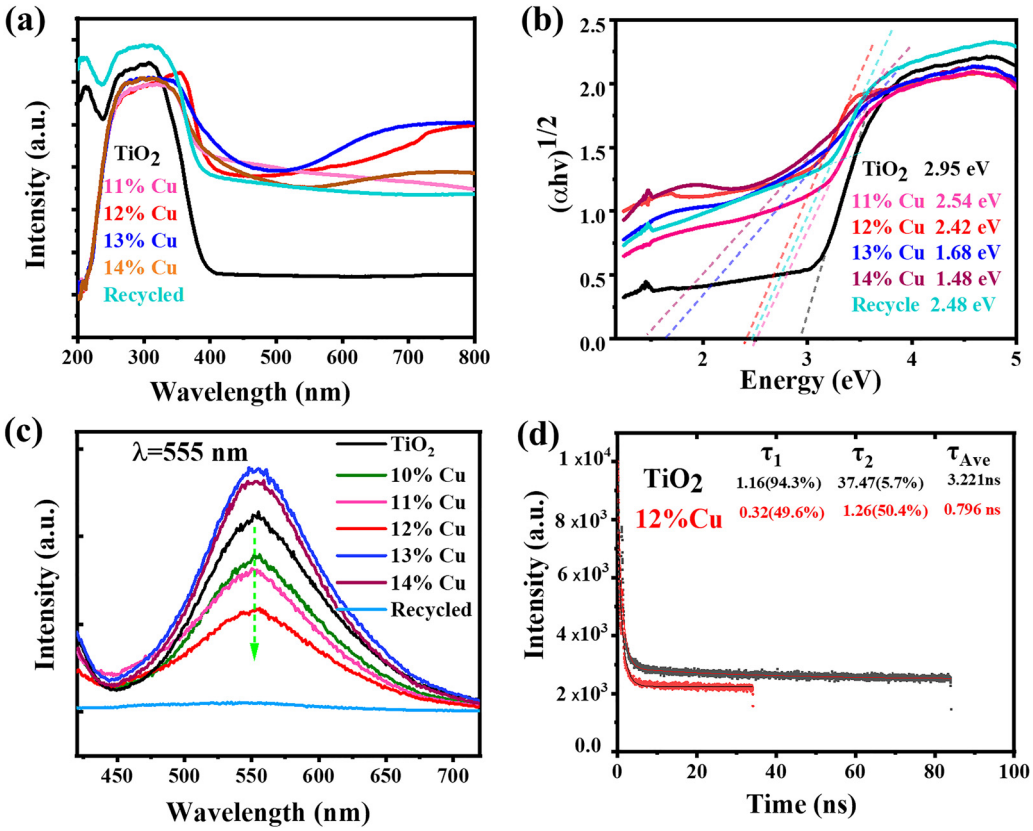

Fig. 4 (a) UV-visible absorption spectra of pristine TiO_2 and Cu–TiO_2 with different doped concentrations. (b) Tauc plot of pristine TiO_2 and Cu-doped TiO_2. (c) PL-spectroscopy of pristine TiO_2 and CuO_x–TiO_2. (d) Low-temperature TRPL spectra of pristine TiO_2 and 12% Cu–TiO_2.

in PL peak intensity upon Cu doping, with 12% Cu–TiO_2 showing the weakest emission, indicating maximum charge separation (Fig. 4c). Time-resolved photoluminescence (TRPL) further confirms charge transfer at the CuO_x–TiO_2 heterojunction, as the fluorescence average lifetime of pristine TiO_2 decreases from 3.2 ns to 0.8 ns for 12% Cu–TiO_2 (Fig. 4d and Fig. S8). This suggests that Cu doping enhances electron extraction from TiO_2, leading to efficient charge separation and electron transfer to Cu sites.[91,93] This charge extraction mechanism is supported by the fact that the reduction potential of Cu^{2+}/Cu^{+} (0.16 V *vs.* NHE) is more positive than the conduction band of TiO_2 (−0.1 V *vs.* NHE), making it possible for CuO to reduce to Cu_2O, which is consistent with the XRD data.[50,91,94]

To further assess the electronic changes at the Cu–TiO_2 interface, ultraviolet photoelectron spectroscopy (UPS) was used to measure the work function and valence band maximum (VBM), and a secondary cutoff shift for pristine and 12% Cu–TiO_2 (Fig. S9). In comparison, the UPS shifts show a lower work function (6.3 to 5.5 eV), a deeper VBM (3.8 to 4.5 eV), and an altered secondary cutoff (14.89 to 15.6 eV), consistent with the Fermi level upshift, enhanced surface metallicity, and a stronger hole oxidation power. This shift likely arises from the formation of Cu^0/Cu^+ species and modified surface dipoles, facilitating easier electron transfer for the HER.[55,95] However, HER performance also depends on the oxidation state of surface Cu species (Cu^0, Cu^+, and Cu^{2+}). These states affect how electrons and holes are trapped or shuttled. That is why XPS is needed to see how these oxidation states change during MPR operation conditions.

2.4. Dynamic oxidation state in the Cu redox cycle and surface reconstruction

X-ray photoelectron spectroscopy (XPS) was conducted to investigate the evolution of Cu oxidation states as a function of Cu doping and to correlate dynamic changes under irradiation with HER activity. The Cu 2p spectra of 12% Cu–TiO_2 exhibited two dominant sets of spin–orbit peaks with associated satellite features (Fig. S10). The first set, at 934.2 eV (Cu $2p_{3/2}$) and 954.2 eV (Cu $2p_{1/2}$), was assigned to Cu^{2+}, while the second set, at 932.9 eV (Cu $2p_{3/2}$) and 952.2 eV (Cu $2p_{1/2}$), was attributed to reduced Cu^0/Cu^+ species, consistent with previous reports.[62,96] An additional peak at 936.0 eV was assigned to $Cu(OH)_2$.

Systematic variations in both binding energy and the Cu $2p_{3/2}$ intensity ratio of Cu^0/Cu^+ to Cu^{2+} were observed as the Cu content increased from 11% to 13%. Compared with 11% Cu–TiO_2, where the ratio of Cu^0/Cu^+ to Cu^{2+} was ∼1 : 1, the relative intensity of Cu^0/Cu^+ increased to ∼2 : 1 at 12% Cu–TiO_2, indicating the growth of reduced Cu species. This was accompanied by a positive shift of 0.5 eV in the Cu^0/Cu^+ peak (from 932.4 eV to 932.9 eV) and a negative shift of 0.7 eV for CuO, consistent with the formation of Cu_2O as also

observed by XRD. At 13% Cu–TiO_2, a negative shift of 0.6 eV was detected for the Cu^0/Cu^+ peak, together with the disappearance of satellite features for Cu^{2+}, reflecting enhanced metallic character due to further reduction to Cu^0. The Cu^{2+} peak at 934.2 eV (12% Cu) further shifted negatively to 934.0 eV (Δ = 0.2 eV), confirming progressive surface reduction with an increase in Cu doping. The corresponding satellite peaks at 940.3 and 943.2 eV, characteristic of CuO, were most prominent at 12% loading, supporting the maximum doping threshold before extensive reduction occurs at 13%. Hence, the approximated concentration trend at the surface found to be: CuO > Cu > Cu_2O (11% Cu–TiO_2), Cu_2O > Cu > CuO (12% Cu–TiO_2), and Cu > Cu_2O > CuO (13% Cu–TiO_2), which is consistent with XRD results. These results confirm the coexistence of Cu^0, Cu_2O, and CuO in 12% Cu–TiO_2 in well-defined ratios, where Cu_2O has the highest concentration and corresponding higher HER activity.

The high-resolution O 1s spectra of pristine TiO_2 and 12% Cu–TiO_2 reveal two deconvoluted peaks at 529.29 eV and 531.8 eV corresponding to lattice oxygen vacancies (Ov) and surface O_{OH}, respectively (Fig. S10d).[90,91] Compared to pristine TiO_2, in 12% Cu–TiO_2, the O_{OH} peak intensity increases from ~30% to 44%, confirming an increase in OH adsorption sites, which facilitate accelerating proton–electron transfer during the HER. The binding energy difference (ΔE_{BE}) between Ov and O_{OH} progressively widens from 1.5 eV in pristine TiO_2 to 2.44 eV (11%), 2.56 eV (12%), and 2.55 eV (13%) in CuO_x–TiO_2. The ΔE_{BE} reaches a maximum of 2.56 eV in 12% Cu–TiO_2 indicating stronger interfacial electronic and dipole interactions between Cu species and the TiO_2 lattice, leading to enhanced stabilization of surface O_{OH} intermediates.[97,98] Notably, the correlation between the ΔE_{BE} increase and the concurrent reduction of Cu^{2+} to Cu^+/Cu^0 (as observed in the Cu 2p spectra) highlights a synergistic effect, wherein Cu redox dynamics enhance charge redistribution at oxygen sites. These findings suggest that the optimal Cu loading of ~12% not only just optimizes the $Cu^0/Cu^+/Cu^{2+}$ ratio but also tunes the electronic environment of oxygen species, thereby promoting HER activity.

The Ti 2p spectra exhibit peaks at 458.54 eV (Ti $2p_{3/2}$) and 464.59 eV (Ti $2p_{1/2}$), which shift toward lower binding energies upon Cu doping: ~0.4 eV in 11% Cu–TiO_2, ~0.47 eV in 12% Cu–TiO_2, and partially reverting to ~0.11 eV in 13% Cu–TiO_2 (Fig. 5b and Fig. S10c). This negative shift is attributed to electron donation from oxygen vacancies, which enhances Ti^{3+} character and modifies the electronic structure of the TiO_2 lattice.[48,69] The trend correlates with the Cu-induced reduction of surface species, suggesting a synergistic effect between Cu doping, Ti^{3+} character, and oxygen vacancy generation, all of which can influence HER activity.

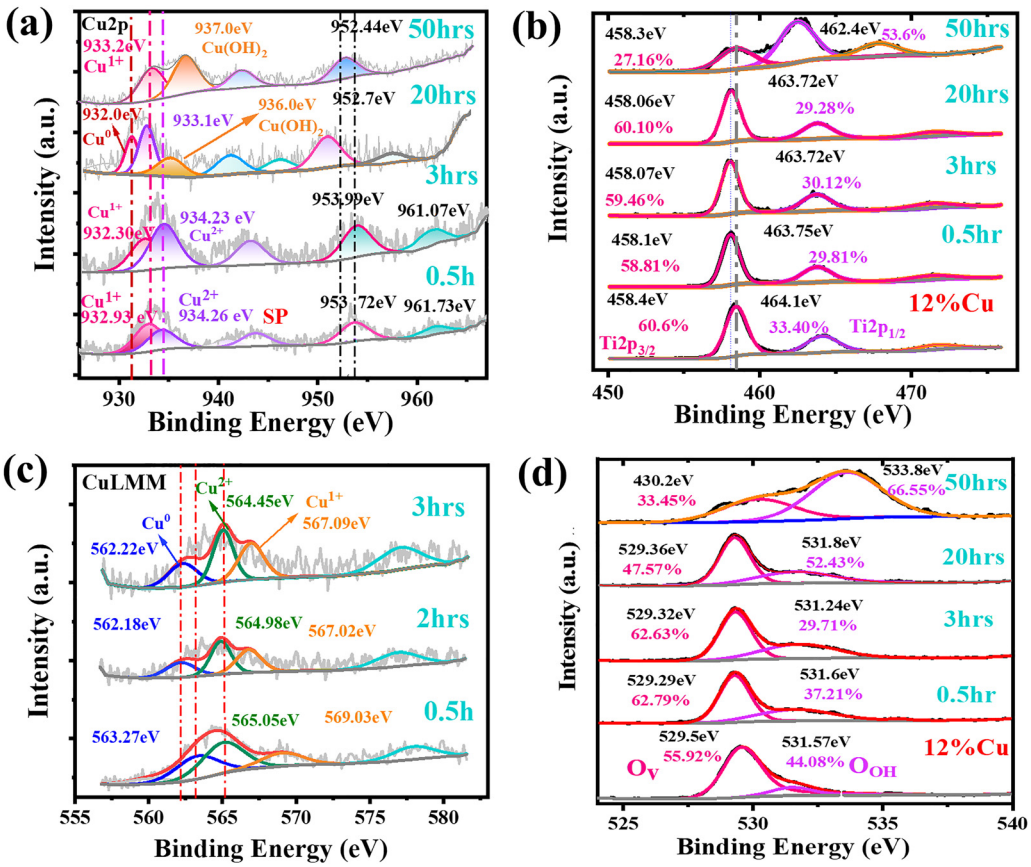

Fig. 5 XPS data analysis for 12% Cu–TiO_2 at different time intervals during photocatalytic HER. (a) Cu $2p_{2/3}$ scan. (b) Ti $2p_{2/3}$ scan. (C) Cu LMM Auger scan. (d) O 1s scan.

Overall, these analyses demonstrate that an optimal Cu loading of ~12% simultaneously optimizes the $Cu^0/Cu^+/Cu^{2+}$ content, enhances surface OH adsorption, and tunes Ti^{4+} and oxygen vacancy states, thereby creating an electronically favorable environment for the HER. Further doping beyond this level leads to minor electronic changes, consistent with diminishing catalytic activity.

Under light irradiation during MPR, the 12% Cu–TiO_2 catalyst exhibits a significantly higher H_2 generation rate (30.6 mmol g^{-1} h^{-1}) compared to 11% (8.0 mmol g^{-1} h^{-1}) and 13% (17.0 mmol g^{-1} h^{-1}). This enhanced performance correlates with the optimized $Cu^0/Cu_2O/CuO$ concentration ratio, increased surface OH availability, and the synergistic interplay among Cu^0, Cu^+, Cu^{2+}, and Ti^{4+} species at the CuO_x–TiO_2 interface.[67,68] Consistent with XRD observations (Fig. 2c), monitoring of Cu $2p_{3/2}$ peaks over 50 h of irradiation reveals dynamic restructuring and redox behavior, which leads to stabilizing Cu_2O (933.2 eV) and $Cu(OH)_2$ (937.0 eV) at the surface (Fig. 5a).[99] The broad Cu $2p_{3/2}$ peak assigned to Cu^+/Cu^0 at 932.9 eV (after 0.5 h) shifted negatively to 932.0 eV (Cu^0) after 20 h, followed by a reversible positive shift to 933.2 eV (Cu^+) after 50 h, demonstrating the reversible $Cu^+ \rightleftharpoons Cu^0$ redox process that stabilizes interfacial Cu_2O. Simultaneously, the Cu $2p_{3/2}$ peak of CuO at 934.2 eV (0.5 h) evolved or overlapped into the concurrent growth of Cu^+ (933.2 eV) and $Cu(OH)_2$ at 937 eV after 50 h of irradiation, demonstrating the reversible $Cu^+ \rightleftharpoons Cu^{2+}$ redox process.[39,100,101] Auger Cu LMM analysis further confirmed the negative shifts in binding energies by 1.05 eV (Cu^0), 1.94 eV (Cu^+), and 0.6 eV (Cu^{2+}) over three hours of irradiation (Fig. 5c).[42,102–104] The negative shifts indicate that photogenerated electrons in TiO_2 are transferred to the Cu dopants, stabilizing Cu_2O at 567 eV, consistent with Cu $2p_{3/2}$ and XRD results (Fig. 2c). Cu^+ ions are most strongly affected, showing that Cu acts as an electron acceptor under irradiation.

After 50 h of irradiation, the O 1s spectra of 12% Cu–TiO_2 exhibit (in addition to the peaks at 530 eV (O_v) and 532 eV (O_{OH})), a third dominant peak at 533.8 eV, assigned to a substantial amount of chemisorbed OH^- (H_2O) groups on the surfaces, consistent with the growth of $Cu(OH)_2$ observed in the Cu $2p_{3/2}$ spectra (Fig. 5d).[105–111] The pronounced $Cu(OH)_2$ signal indicates efficient water dissociation at the Cu sites, a favorable feature for H_2 generation in aqueous media.[98] Furthermore, the ΔE_{BE} between O_v and the predominant chemisorbed O_{OH} increased to 3.6 eV after 50 h of irradiation (Fig. 5d), indicating that the O_{OH} sites became more electron-poor. This electronic polarization of surface hydroxyls can enhance water adsorption, thereby promoting HER activity.[59,112,113] In the Ti $2p_{3/2}$ spectra, the BE initially decreased by 0.34 eV after 20 h of irradiation and subsequently increased by 0.30 eV after 50 h of irradiation (Fig. 5b), aligned with Cu $2p_{3/2}$ peaks. The initial negative shift is consistent with increased Ti^{3+} character, reflecting a more reducing surface environment as methanol scavenges photogenerated holes and promotes electron accumulation. The Ti $2p_{3/2}$ peak broadened and became asymmetrical, which also suggests the formation of non-stoichiometric TiO_{2-x} (CuO → Cu_2O conversion) and/or partially reduced Ti^{3+} species.[114] The Ti $2p_{3/2}$ positive shift may be due to the contribution of surface Ti^{3+} in the conversion of Cu^{2+} to Cu^{1+} and reduces its reducing character (Fig. 5b). The positive shift in Ti $2p_{3/2}$ may also be due to the increased presence of $Cu(OH)_2$ species on the surface, which may introduce a strong dipole moment or local electric field.[33,65,90,115,116] Surprisingly, an abnormal change in $2p_{3/2}/2p_{1/2}$ intensity ratio (~2 : 1) was observed as a result of attenuation of the $2p_{3/2}$ signal, which may be due to accumulation of dynamic Cu_2O, $Cu(OH)_2$, and OH^- at the surface, segregation of Cu species or overlapping of other species at the $2p_{1/2}$ peak position.[114,117]

These trends suggest a zwitterionic electrostatic polarization effect due to an unexpectedly large amount of OH^- in the Cu–TiO_2 aqueous solution (despite near-neutral pH) that can only be explained by water dissociation.[98] Consequently, Ti–O or Cu–O bonds cooperate to stabilize intermediates where the electron-rich O_v and polarized OH groups create synergistic active sites that enhance charge separation, improve adsorption of H_2O and H^+, and facilitate HER kinetics.[59,112] Contrarily, as a trade-off, while $Cu(OH)_2$ enrichment enhances surface reactivity, it also leads to the formation of a dense ''insulating or diffusion layer'' that can block light penetration and impede reactant access to the underlying active TiO_2 sites.[97,98] Additionally, Cu segregation may also reduce the effective participation of TiO_2 in photocatalysis by limiting light absorption and decreasing the generation of photogenerated charge carriers, ultimately impairing the overall efficiency of the photocatalyst.[59, 112]Hence, the abundance of hydroxyl groups (–OH) renders the surface more oxidative, potentially influencing methanol oxidation during the HER.[118] Consequently, these findings highlight the reversible dynamic redox behavior of CuO_x species (CuO ⇆ Cu_2O ⇆ Cu) and their role in thermodynamically and kinetically stable $Cu(OH)_2$ and Cu_2O towards optimized HER performance.[40,119]

2.5. Photocatalytic hydrogen evolution performance

The photocatalytic hydrogen evolution reaction (HER) was systematically evaluated for pristine TiO_2 and 1–14% Cu-doped TiO_2 samples under Xe lamp irradiation, using 20% methanol as a sacrificial hole scavenger (Fig. 6 and Fig. S11–S13). All Cu-doped catalysts outperformed pristine TiO_2 (3.3 mmol g^{-1} h^{-1}), with the 12% Cu–TiO_2 sample achieving a highest rate of 30.6 ± 2 mmol g^{-1} h^{-1}—tenfold higher than that of pristine TiO_2 (Fig. 6a). The superior performance of 12% Cu–TiO_2 compared to 11% and 13% loadings arises from a favorable balance of porosity, $Cu^0/Cu_2O/CuO$ concentration ratio, charge-transfer efficiency, and oxygen-vacancy defects, as confirmed by BET (Fig. S4), XPS (Fig. 5 and Fig. S10), PL (Fig. 4c), and XRD (Fig. 2a). At 11% doping, the CuO/Cu_2O ratio is higher relative to the optimal 12% sample (XPS, Fig. S10b), reducing the fraction of catalytically active Cu_2O. At 13% doping, the Cu^0/Cu^{+1} ratio is higher, which leads to Cu^0 aggregation and clustering that clogs mesopores, reduces pore volume, and partially blocks photocatalytic sites. BET analysis confirmed that the pore volume of 12% Cu–TiO_2 (0.31 cm^3 g^{-1}) exceeds that of both 11% (0.23 cm^3 g^{-1}) and 13%

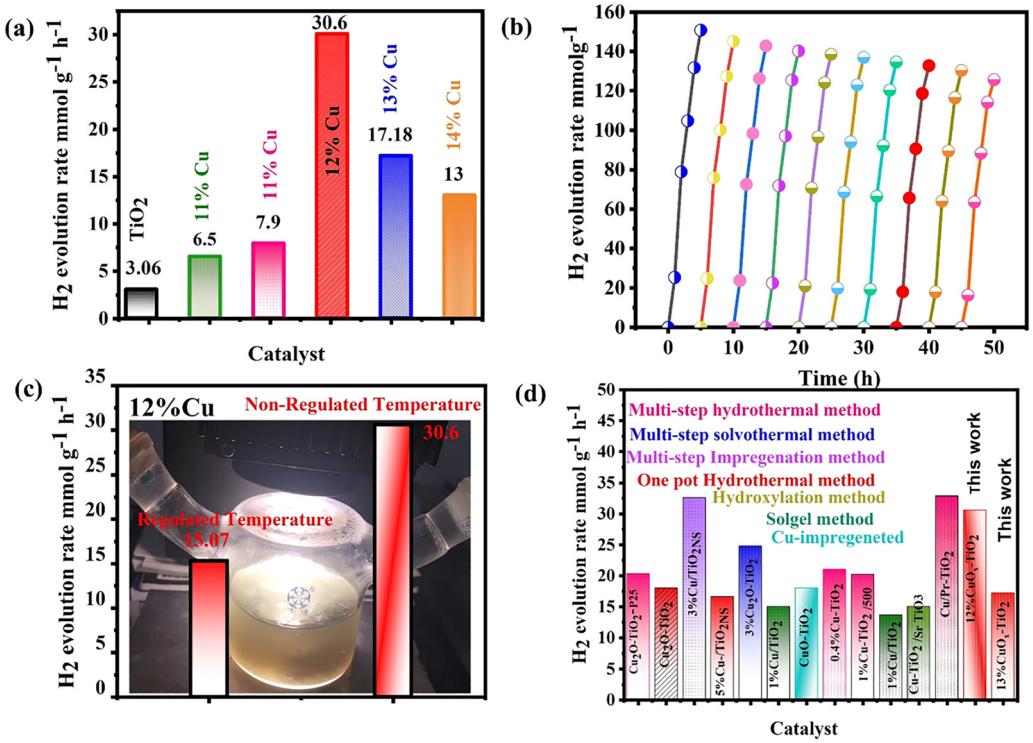

Fig. 6 H_2 evolution rate (HER) of pristine TiO_2 and CuO_x–TiO_2 in the 20% methanol in water system. (a) HER of pristine TiO_2 and 10–14% Cu–TiO_2. (b) Stability test in 10 cycles (50 h.). (c) HER of 12% Cu–TiO_2 at regulated temperature. (d) High-performing methanol photo reforming HER rate for CuO_x–TiO_2 and color-coded synthesis methods from Table S2.

(0.21 cm^3 g^{-1}), in good agreement with HER activity trends (Table S2).[65,120] This effect is further supported by PL measurements, where 12% Cu–TiO_2 shows the most pronounced quenching of emission intensity, consistent with its higher Cu_2O fraction and more efficient electron extraction (Fig. 4c).[63,121]

The long-term stability and recyclability of 12% Cu–TiO_2 were assessed over 50 h of continuous irradiation (10 cycles of 5 h), with >90% retention in the hydrogen evolution rate (Fig. 6b and Fig. S11). Control experiments conducted at 20 °C under identical conditions ruled out thermal contributions, giving a reduced HER rate of 15 mmol g^{-1} h^{-1} (Fig. 6c and Fig. S13). Furthermore, 100% recovery of activity was observed after replenishment of 20% methanol following 15 h of operation (Fig. S13c), confirming methanol's essential role in sustaining performance. Finally, the optimized 12% Cu–TiO_2 exhibited an apparent quantum efficiency (AQE) of 9.7% at 450 nm (Fig. S14), reflecting efficient utilization of monochromatic visible light.

2.6. Charge transfer mechanism and the corrosion–healing redox loop cycle

Under photocatalytic conditions, the interfacial dynamics of CuO, Cu_2O, and metallic Cu in CuO_x–TiO_2 heterostructures are governed by the heterojunction configuration, band alignment, and charge-transfer pathways. The most plausible mechanism follows an S-scheme model, in which band bending and internal electric fields direct carrier separation, with metallic Cu acting as an efficient cocatalyst (Fig. 7). This assignment is substantiated by steady-state and time-resolved PL, XRD, XPS, and UPS analyses (Fig. 2c, 4c, d, 5a, c and Fig. S9) and is consistent with prior literature.[122,123] For 12% CuO_x–TiO_2, photoluminescence quenching and the reduction of the average TRPL lifetime from 3.2 ns (pristine TiO_2) to 0.8 ns (Fig. 4d) demonstrate accelerated electron extraction by Cu sites. Concurrently, UPS spectra show a work function decrease from 6.3 to 5.5 eV, indicative of enhanced metallic character (Cu^0/Cu^+ species) and improved surface electron transfer kinetics for hydrogen evolution. XPS reveals negative shifts in the Cu $2p_{3/2}$ binding energies, corroborating electron transfer into Cu redox states (Cu^{2+} → Cu^+ → Cu^0), while XRD and XPS confirm the light-induced reduction of Cu^{2+} to Cu_2O and metallic Cu (Fig. 2c and 5a).[8]

Within the S-scheme framework, photogenerated e^- in the TiO_2 CB and h^+ in the Cu_2O VB undergo interfacial selective recombination of low-energy carriers, while the remaining high-energy carriers (e^- in the Cu_2O CB and h^+ in the TiO_2 VB) drive hydrogen evolution and methanol oxidation, respectively.[123–125] This pathway effectively suppresses overoxidation of Cu^+ to Cu^{2+}, thereby limiting the formation of CuO/$Cu(OH)_2$ and stabilizing the Cu_2O phase. Simultaneously, metallic Cu establishes Schottky junctions with TiO_2 that collect high energy CB electrons and preferably catalyze proton reduction, preventing the over-reduction of Cu_2O. The dynamic

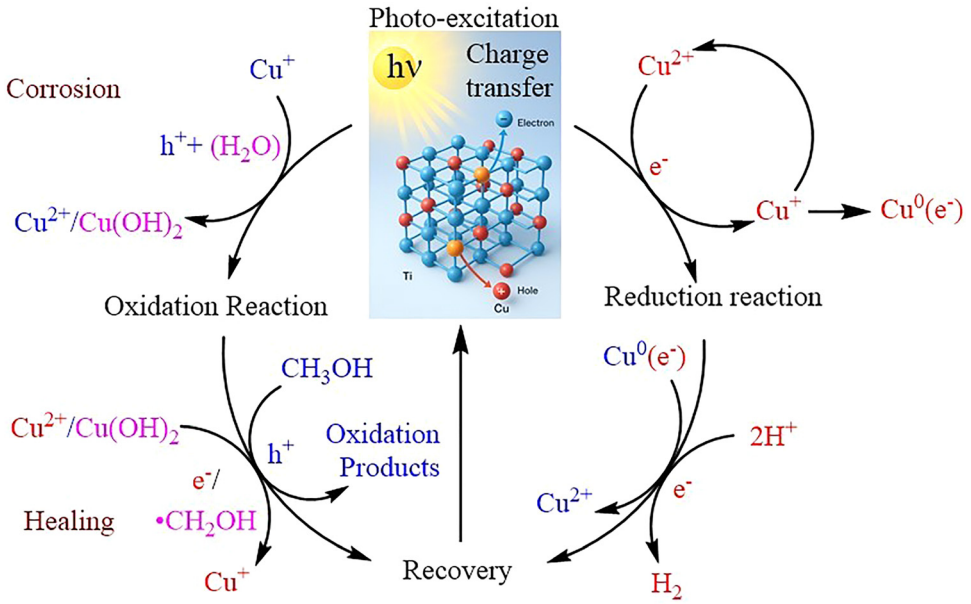

Fig. 7 The proposed photocatalytic hydrogen evolution reaction (HER) mechanism (corrosion–healing redox loop) over 12% CuO_x–TiO_2 in the presence of methanol and water.[23,39]

$Cu^{2+}/Cu^{+}/Cu^{0}$ redox cycle, confirmed by Cu LMM spectra (Fig. 5c), facilitates efficient charge transport and underpins the enhanced HER activity and long-term durability of the composite catalyst (Fig. 7).[23,122,126]

Under prolonged irradiation in 20% methanol, both Cu_2O and $Cu(OH)_2$ continue to grow due to a self-sustaining corrosion–healing redox loop at the Cu_2O–TiO_2 interface.[39] In this process, holes reaching Cu_2O oxidize Cu^{+} to Cu^{2+}, which hydrolyzes to $Cu(OH)_2$, while electrons and methanol-derived intermediates (such as $^{\bullet}CH_2OH$ or formaldehyde) favoring reduction of transient $Cu(OH)_2$ back to Cu_2O at other locations. Because these oxidation and reduction events occur at different sites and time, XPS and XRD may show concurrent growth of Cu^{+} and Cu^{2+} species despite originating from the same redox cycling. However, this loop consumes photogenerated carriers inefficiently, introduces recombination centers, and accumulates insulating $Cu(OH)_2$ deposits that progressively shift the system toward mimicking type-II–like charge separation with higher recombination probability. The result has diminished hydrogen evolution activity.[127]

Nevertheless, the Cu^{+}/Cu^{2+} redox couple also functions as a dynamic electron shuttle, mediating charge transfer while buffering the copper oxidation state under continuous photoirradiation. This redox buffering suppresses irreversible Cu_2O oxidation, while TiO_2 serves as both a structural matrix and electronic stabilizer, dissipating excess charge and mitigating rapid degradation of the Cu-based species. To maintain efficient H_2 evolution, continuous supply/addition of 20% methanol as a sacrificial agent is required (Fig. S13c). Its oxidation products act as rapid hole scavengers, ensuring reductive equivalents are delivered to transient $Cu(OH)_2$ sites, limiting their accumulation and restoring Cu_2O.

In summary, the proposed S-scheme Cu_2O–TiO_2(101) heterojunction, synergistically coupled with metallic Cu as an electron sink, provides the most consistent mechanistic framework with the experimental observations. This model explains the stabilization of Cu_2O(111) and the controlled presence of $Cu(OH)_2$ under prolonged irradiation, while simultaneously accounting for enhanced charge separation, efficient methanol oxidation, and sustained hydrogen evolution activity.[123]

2.7. Density functional theory (DFT) insights into hydrogen adsorption and stability

To rationalize the experimentally observed enhancement in the HER activity of Cu–TiO_2 systems, we performed density functional theory (DFT) calculations to probe structural, electronic, and catalytic properties. Anatase TiO_2(101) and (001) facets were considered, followed by construction of Cu-doped, CuO–TiO_2(101), and Cu_2O–TiO_2(101) models (Fig. 8a, 9a and Fig. S15–S19). Projected density of states (PDOS) analysis revealed strong hybridization between Cu-3d and Ti-3d/O-2p orbitals, with the d-band centers (ε_d) of Cu–TiO_2(101) lying closer to the Fermi level (0.81 eV) compared to Cu–TiO_2(001) (1.91 eV) (Fig. 8b). This shift indicates stronger hydrogen adsorption at the (101) surface, in line with its superior HER activity. Charge density difference (CDD) maps further confirmed greater electron accumulation around Cu on (101), with Bader analysis showing higher charge transfer (1.41 e) relative to the (001) surface (0.71 e) (Fig. 8c).

The calculated Gibbs free energy (ΔG_{H^*}) profiles provide a direct comparison with HER benchmarks. Cu–TiO_2(101) exhibits a nearly thermoneutral hydrogen adsorption energy ($\Delta G_{H^*} = -0.06$ eV), closely matching Pt(111) (−0.09 eV), whereas Cu–TiO_2(001) shows stronger binding ($\Delta G_{H^*} = -0.65$ eV), which

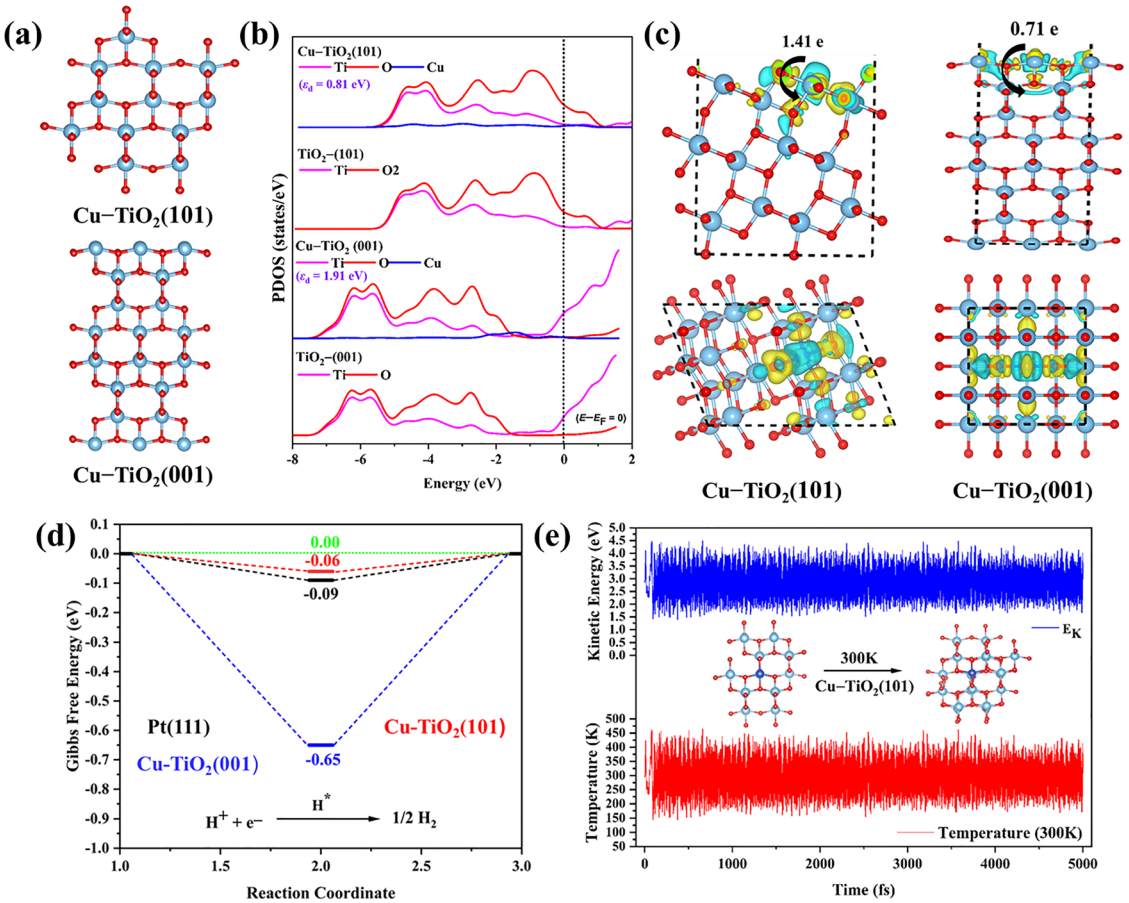

Fig. 8 (a) Cu–TiO_2 surface at two phases at 101 and 001, (b) the PDOS plots of pristine and newly adopted models, (c) charge density differences (CDDs) of investigated surfaces, (d) ΔG_{H^*} of Cu–TiO_2 at (101) and (001) phase comparison with experimental Pt(111), and (e) AIMD simulations showing the thermal stability of the Cu–TiO_2(101) phase.

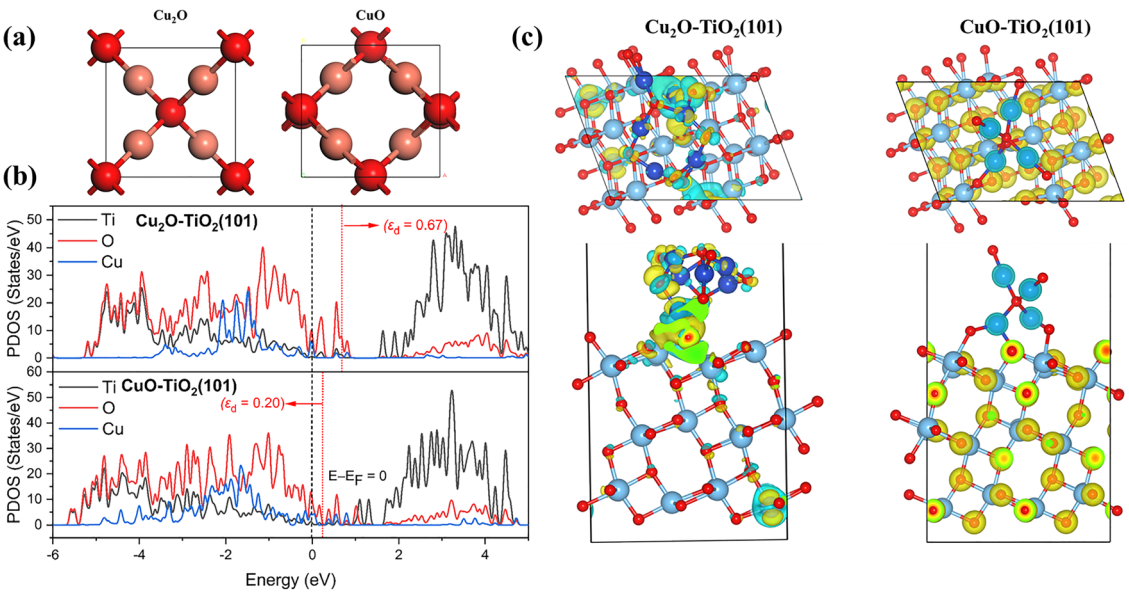

Fig. 9 (a) Structural configuration of CuO and Cu_2O, (b) the PDOS plots of CuO–TiO_2(101), and Cu_2O–TiO_2(101), and (c) charge density differences of CuO–TiO_2(101) and Cu_2O–TiO_2(101).

hinders H_2 desorption (Fig. 8d). *Ab initio* molecular dynamics (AIMD) simulations confirmed the thermal stability of Cu–TiO_2(101) at 300 K (Fig. 8e). These theoretical findings support the experimental observation that Cu–TiO_2(101) serves as the most active HER interface.

To further assess the role of Cu oxidation states, CuO–TiO_2(101) and Cu_2O–TiO_2(101) models were constructed (Fig. 9a). PDOS and CDD analyses (Fig. 9b and c) show distinct charge redistribution, with Bader charges of 0.73 e and 0.84 e, respectively, compared to 1.41 e for metallic Cu. Correspondingly, ΔG_{H^*} values follow the order: Cu–TiO_2(101) (−0.06 eV) > Cu_2O–TiO_2(101) (−1.37 eV) > CuO–TiO_2(101) (+1.20 eV), indicating that metallic Cu provides the most favourable H adsorption–desorption balance (Fig. S19). This agrees with experimental evidence where metallic Cu functions as an electron sink, Cu^+/Cu^{2+} acts as a redox mediator, and TiO_2 stabilizes the composite against irreversible oxidation.

Overall, the DFT results corroborate the proposed charge transfer mechanism by demonstrating that (i) Cu doping lowers the work function and enhances electron transfer, (ii) Cu–TiO_2(101) offers the most optimal hydrogen binding energy among all tested models, and (iii) the oxidation state of Cu critically tunes HER activity, with metallic Cu enabling efficient electron transfer and HER kinetics.

3. Conclusion

This study presents a one-pot scalable strategy for CuO_x–TiO_2 photocatalysts, achieving a record HER rate of 30.6 mmol g^{-1} h^{-1} with excellent durability and scalability. Beyond the dynamic CuO ⇆ Cu_2O ⇆ Cu^0 redox cycle, we identify for the first time a corrosion–healing redox loop, wherein Cu_2O is continually regenerated *via* reversible oxidation to CuO/$Cu(OH)_2$ and reduction by methanol-derived intermediates. This self-healing process stabilizes active sites, suppresses irreversible deactivation, and underpins the long-term photocatalytic stability. An S-scheme heterojunction charge transfer pathway combined with DFT validation of near-Pt-like hydrogen binding energetics on Cu–TiO_2(101) position Cu-based systems as strong contenders to replace noble metals for photocatalytic hydrogen production. The demonstrated structural robustness, scalability, and redox self-healing open a new avenue for designing durable and economically viable solar-to-hydrogen catalysts.

Conflicts of interest

The authors declare no conflicts of interest.

Data availability

The data supporting this article have been included as part of the supplementary information (SI). Supplementary information: XRD, SEM, XPS, BET, and DFT measurements data. See DOI: **https://doi.org/10.1039/d5mh01679g**.

Acknowledgements

The authors are grateful for the financial supports of the Natural Science Foundation of China (Grant No: 12174092 and U21A20500), Overseas Expertise Introduction Center for Discipline Innovation (D18025), and Manchester Metropolitan University research accelerator grant (Project ID: 5196865).

References

1 A. Majumdar, J. M. Deutch, R. S. Prasher and T. P. Griffin, *Joule*, 2021, **5**, 1905–1908.
2 M. Newborough and G. Cooley, *Fuel Cells Bull.*, 2020, 16–22.
3 S. Wu, N. Salmon, M. M.-J. Li, R. Bañares-Alcántara and S. C. E. Tsang, *ACS Energy Lett.*, 2022, **7**, 1021–1033.
4 I. I. E. Agency, IEA-Global Hydrogen Review-2023, 2023.
5 I.-I. R. E. Agency, IRENA-World energy transitions Outlook *2022- 1.50C Pathway*.
6 D. R. Palo, R. A. Dagle and J. D. Holladay, *Chem. Rev.*, 2007, **107**, 3992–4021.
7 A. M. Ranjekar and G. D. Yadav, *Ind. Eng. Chem. Res.*, 2021, **60**, 89–113.
8 S. Luo, H. Song, F. Ichihara, M. Oshikiri, W. Lu, D.-M. Tang, S. Li, Y. Li, Y. Li, P. Davin, T. Kako, H. Lin and J. Ye, *J. Am. Chem. Soc.*, 2023, **145**, 20530–20538.
9 S. R. Arsad, P. J. Ker, M. A. Hannan, S. G. Tang, N. RS, C. F. Chau and T. M. Mahlia, *Int. J. Hydrogen Energy*, 2024, **50**, 447–472.
10 P. Albertus, J. S. Manser and S. Litzelman, *Joule*, 2020, **4**, 21–32.
11 B. E. Lebrouhi, J. J. Djoupo, B. Lamrani, K. Benabdelaziz and T. Kousksou, *Int. J. Hydrogen Energy*, 2022, **47**, 7016–7048.
12 H. Nishiyama, T. Yamada, M. Nakabayashi, Y. Maehara, M. Yamaguchi, Y. Kuromiya, Y. Nagatsuma, H. Tokudome, S. Akiyama, T. Watanabe, R. Narushima, S. Okunaka, N. Shibata, T. Takata, T. Hisatomi and K. Domen, *Nature*, 2021, **598**, 304–307.
13 T. Hisatomi and K. Domen, *Nat. Catal.*, 2019, **2**, 387–399.
14 J. H. Kim, D. Hansora, P. Sharma, J.-W. Jang and J. S. Lee, *Chem. Soc. Rev.*, 2019, **48**, 1908–1971.
15 Y. Goto, T. Hisatomi, Q. Wang, T. Higashi, K. Ishikiriyama, T. Maeda, Y. Sakata, S. Okunaka, H. Tokudome, M. Katayama, S. Akiyama, H. Nishiyama, Y. Inoue, T. Takewaki, T. Setoyama, T. Minegishi, T. Takata, T. Yamada and K. Domen, *Joule*, 2018, **2**, 509–520.
16 S. Guo, X. Li, J. Li and B. Wei, *Nat. Commun.*, 2021, **12**, 1343.
17 P. Zhou, I. A. Navid, Y. Ma, Y. Xiao, P. Wang, Z. Ye, B. Zhou, K. Sun and Z. Mi, *Nature*, 2023, **613**, 66–70.
18 H. Meng, Y. Yang, T. Shen, Z. Yin, L. Wang, W. Liu, P. Yin, Z. Ren, L. Zheng, J. Zhang, F.-S. Xiao and M. Wei, *Nat. Commun.*, 2023, **14**, 7980.
19 S. P. Shelake, D. N. Sutar, B. M. Abraham, T. Banerjee, A. V. S. Sainath and U. Pal, *Adv. Funct. Mater.*, 2024, **34**, 2403795.

20 O. F. Aldosari and I. Hussain, *Int. J. Hydrogen Energy*, 2024, **59**, 958–981.
21 A. Zaleska, *Recent Pat. Eng.*, 2008, **2**, 157–164.
22 A. Khlyustova, N. Sirotkin, T. Kusova, A. Kraev, V. Titov and A. Agafonov, *Mater. Adv.*, 2020, **1**, 1193–1201.
23 M. Marica, A. Roberto, C. Laura, S. Ilaria and M. Raffaele, *Int. J. Hydrogen Energy*, 2020, **45**, 28531–28552.
24 G. Liu, C. Sun, H. G. Yang, S. C. Smith, L. Wang, G. Q. M. Lu and H.-M. Cheng, *Chem. Commun.*, 2010, **46**, 755–757.
25 T. Morikawa, S. Sato, K. Sekizawa, T. Arai and T. M. Suzuki, *ChemSusChem*, 2019, **12**, 1807–1824.
26 E. B. Aydın, S. Ateş and G. Sığırcık, *Int. J. Hydrogen Energy*, 2022, **47**, 6519–6534.
27 Y. Zuo, S. Bellani, G. Saleh, M. Ferri, D. V. Shinde, M. I. Zappia, J. Buha, R. Brescia, M. Prato and R. Pascazio, *J. Am. Chem. Soc.*, 2023, **145**, 21419–21431.
28 S. M. Thabet, H. N. Abdelhamid, S. A. Ibrahim and H. M. El-Bery, *Sci. Rep.*, 2024, **14**, 10115.
29 M. M. Momeni, N. Mohammadi and M. Mirhosseini, *J. Mater. Sci.: Mater. Electron.*, 2016, **27**, 10147–10156.
30 X. Zhao, P. Wang, Z. Yan and N. Ren, *Chem. Phys. Lett.*, 2014, **609**, 59–64.
31 C. Cheng, W.-H. Fang, R. Long and O. V. Prezhdo, *JACS Au*, 2021, **1**, 550–559.
32 V. Thi Quyen, K. Jitae, P. Thi Huong, L. Thi Thu Ha, D. My Thanh, N. Minh Viet and P. Quang Thang, *Sol. Energy*, 2021, **218**, 150–156.
33 L. Li, X. Chen, X. Quan, F. Qiu and X. Zhang, *ACS Omega*, 2023, **8**, 2723–2732.
34 K. Lalitha, G. Sadanandam, V. D. Kumari, M. Subrahmanyam, B. Sreedhar and N. Y. Hebalkar, *J. Phys. Chem. C*, 2010, **114**, 22181–22189.
35 W. Y. Cheng, T. H. Yu, K. J. Chao and S. Y. Lu, *ChemCatChem*, 2014, **6**, 293–300.
36 Y. Liu, B. Zhang, L. Luo, X. Chen, Z. Wang, E. Wu, D. Su and W. Huang, *Angew. Chem., Int. Ed.*, 2015, **54**, 15260–15265.
37 A. Zindrou, L. Belles, M. Solakidou, N. Boukos and Y. Deligiannakis, *Sci. Rep.*, 2023, **13**, 13999.
38 W. Zhen, W. Jiao, Y. Wu, H. Jing and G. Lu, *Catal. Sci. Technol.*, 2017, **7**, 5028–5037.
39 H. Wang, H. Qi, X. Sun, S. Jia, X. Li, T. J. Miao, L. Xiong, S. Wang, X. Zhang, X. Liu, A. Wang, T. Zhang, W. Huang and J. Tang, *Nat. Mater.*, 2023, **22**, 619–626.
40 C. Y. Toe, Z. Zheng, H. Wu, J. Scott, R. Amal and Y. H. Ng, *Angew. Chem., Int. Ed.*, 2018, **57**, 13613–13617.
41 J.-K. Lee, S. Wu, P. C. Lim and Z. Zhang, *Nano Lett.*, 2022, **22**, 4654–4660.
42 J. Hu, X. Shen, A. Liu, Z. Lu, J. Xie, A. Hao, X. Jiang, J. Wang and Y. Cao, *J. Mater. Chem. A*, 2023, **11**, 1290–1300.
43 Q. Hou, J. Buckeridge, A. Walsh, Z. Xie, Y. Lu, T. W. Keal, J. Guan, S. M. Woodley, C. R. A. Catlow and A. A. Sokol, *Front. Chem.*, 2021, **9**, 780935.
44 J. P. Yasomanee and J. Bandara, *Sol. Energy Mater. Sol. Cells*, 2008, **92**, 348–352.
45 H. Yang, Y. Chen, X. Cui, G. Wang, Y. Cen, T. Deng, W. Yan, J. Gao, S. Zhu, U. Olsbye, J. Wang and W. Fan, *Angew. Chem., Int. Ed.*, 2018, **57**, 1836–1840.
46 A. Li, D. Yao, Y. Yang, W. Yang, Z. Li, J. Lv, S. Huang, Y. Wang and X. Ma, *ACS Catal.*, 2022, **12**, 1315–1325.
47 J. Cao, J. Zhang, W. Guo, H. Chen, J. Li, D. Jing, B. Luo and L. Ma, *Ind. Eng. Chem. Res.*, 2023, **62**, 1310–1321.
48 T. Wei, Y.-N. Zhu, X. An, L.-M. Liu, X. Cao, H. Liu and J. Qu, *ACS Catal.*, 2019, **9**, 8346–8354.
49 L. Chang, S. T. Yong, S. P. Chai, L. K. Putri, L. L. Tan and A. R. Mohamed, *Mater. Today Chem.*, 2023, **27**, 101334.
50 Y. Zhang, J. Zhao, H. Wang, B. Xiao, W. Zhang, X. Zhao, T. Lv, M. Thangamuthu, J. Zhang and Y. Guo, *Nat. Commun.*, 2022, **13**, 58.
51 B. Xiao, C. Shen, Z. Luo, D. Li, X. Kuang, D. Wang, B. Zi, R. Yan, T. Lv, T. Zhou, J. Zhang and Q. Liu, *Chem. Eng. J.*, 2023, **468**, 143650.
52 I. Majeed, M. A. Nadeem, A. Badshah, F. K. Kanodarwala, H. Ali, M. A. Khan, J. A. Stride and M. A. Nadeem, *Catal. Sci. Technol.*, 2017, **7**, 677–686.
53 B.-H. Lee, S. Park, M. Kim, A. K. Sinha, S. C. Lee, E. Jung, W. J. Chang, K.-S. Lee, J. H. Kim, S.-P. Cho, H. Kim, K. T. Nam and T. Hyeon, *Nat. Mater.*, 2019, **18**, 620–626.
54 S. Hejazi, S. Mohajernia, B. Osuagwu, G. Zoppellaro, P. Andryskova, O. Tomanec, S. Kment, R. Zbořil and P. Schmuki, *Adv. Mater.*, 2020, **32**, 1908505.
55 C. W. Lee, B.-H. Lee, S. Park, Y. Jung, J. Han, J. Heo, K. Lee, W. Ko, S. Yoo, M. S. Bootharaju, J. Ryu, K. T. Nam, M. Kim and T. Hyeon, *Nat. Mater.*, 2024, **23**, 552–559.
56 M. González-Tejero, J. G. Villachica-Llamosas, A. Ruiz-Aguirre and G. Colón, *ACS Appl. Energy Mater.*, 2023, **6**, 4007–4015.
57 B. Zi, H. Zheng, T. Zhou, Q. Lu, M. Chen, B. Xiao, Y. Zhang, Z. Qiu, H. Sun, J. Zhao, Z. Luo, T. He, J. Zhang, Z. Zhao and Q. Liu, *Small*, 2024, **20**, 2305779.
58 J. Li, J. Hu, M. Zhang, W. Gou, S. Zhang, Z. Chen, Y. Qu and Y. Ma, *Nat. Commun.*, 2021, **12**, 3502.
59 C. Xing, Z. Zhang, Y. Zhang, X. Han, L. Yang, J. Li, X. Wang, P. Martinez, M. Demir, L. Piveteau, P. Florian, J. Arbiol, Y. Guo, J. Llorca and A. Cabot, *Mater. Today Nano*, 2023, **24**, 100435.
60 I. T. McCrum and M. T. M. Koper, *Nat. Energy*, 2020, **5**, 891–899.
61 Y. Cao, Z. Chen, P. Li, A. Ozden, P. Ou, W. Ni, J. Abed, E. Shirzadi, J. Zhang, D. Sinton, J. Ge and E. H. Sargent, *Nat. Commun.*, 2023, **14**, 2387.
62 J. Yu and J. Ran, *Energy Environ. Sci.*, 2011, **4**, 1364–1371.
63 G. Li, J. Huang, Z. Deng, J. Chen, Q. Huang, Z. Liu, W. Guo and R. Cao, *Cryst. Growth Des.*, 2019, **19**, 5784–5790.
64 B.-H. Lee, S. Park, M. Kim, A. K. Sinha, S. C. Lee, E. Jung, W. J. Chang, K.-S. Lee, J. H. Kim and S.-P. Cho, *Nat. Mater.*, 2019, **18**, 620–626.
65 G. Sadanandam, X. Luo, X. Chen, Y. Bao, K. P. Homewood and Y. Gao, *Appl. Surf. Sci.*, 2021, **541**, 148687.

66 S. Rajendran, S. S. Mani, T. R. Nivedhitha, A. K. Asoka, P. S. Arun, T. Mathew and C. S. Gopinath, *ACS Appl. Energy Mater.*, 2024, **7**, 104–116.
67 F. Yang, M. Liu, X. Chen, Z. Xu and H. Zhao, *Solar RRL*, 2018, **2**, 1800215.
68 S. Docao, A. R. Koirala, M. G. Kim, I. C. Hwang, M. K. Song and K. B. Yoon, *Energy Environ. Sci.*, 2017, **10**, 628–640.
69 Y. Zhao, Y. Zhao, R. Shi, B. Wang, G. I. N. Waterhouse, L.-Z. Wu, C.-H. Tung and T. Zhang, *Adv. Mater.*, 2019, **31**, 1806482.
70 T. Xu, H. Zheng and P. Zhang, *J. Hazard. Mater.*, 2020, **388**, 121746.
71 M. Zou, M. Wang, J. Wang, D. Zhu, J. Liu, J. Wang, Q. Xiao and J. Chen, *Nanomaterials*, 2023, **13**, 1859.
72 G. Cheng, X. Liu, X. Song, X. Chen, W. Dai, R. Yuan and X. Fu, *Appl. Catal., B*, 2020, **277**, 119196.
73 S. Dolabella, A. Borzì, A. Dommann and A. Neels, *Small Methods*, 2022, **6**, 2100932.
74 J. M. Valero, S. Obregón and G. Colón, *ACS Catal.*, 2014, **4**, 3320–3329.
75 H. Sokoidanto, A. Taufik and R. Saleh, *J. Phys.:Conf. Ser.*, 2020, **1442**(1), 012008.
76 Z. Bai, D. He, S. Fu, Q. Miao, S. Liu, M. Huang, K. Zhao, Y. Wang and X. Zhang, *Nano Select*, 2022, **3**, 1112–1122.
77 J. Ma, R. Yang and H. Chen, *Nat. Commun.*, 2021, **12**, 2314.
78 M. Blencowe, *Nature*, 2016, **530**, 284–285.
79 C. Pornrungroj, A. B. Mohamad Annuar, Q. Wang, M. Rahaman, S. Bhattacharjee, V. Andrei and E. Reisner, *Nature Water*, 2023, **1**, 952–960.
80 A. Asrai, M. Razali, K. Amin and U. Osman, *Dig. J. Nanomater. Biostructures*, 2023, **18**(3), 1105.
81 H. Hamad, E. Bailón-García, F. J. Maldonado-Hódar, A. F. Pérez-Cadenas, F. Carrasco-Marín and S. Morales-Torres, *Appl. Catal., B*, 2019, **241**, 385–392.
82 R. M. Ali, M. R. Elkatory and H. A. Hamad, *Fuel*, 2020, **268**, 117297.
83 M. Sahu and P. Biswas, *Nanoscale Res. Lett.*, 2011, **6**, 1–14.
84 Y. Cao, G. Wang, Q. Ma and Z. Jin, *Dalton Trans.*, 2020, **49**, 1220–1231.
85 M. Tang, D. Yang, J. Wang, Q. Zhou, X. Zhu and Y. Jiao, *Mater. Res. Express*, 2021, **8**, 085007.
86 H. Qian, B. Yuan, Y. Liu, R. Zhu, W. Luan and C. Zhang, *iScience*, 2024, **27**, 109578.
87 Y. Pan, Y. Wang, S. Wu, Y. Chen, X. Zheng and N. Zhang, *Molecules*, 2021, **26**, 6221.
88 J. Xu, D. Gao, H. Yu, P. Wang, B. Zhu, L. Wang and J. Fan, *Chin. J. Catal.*, 2022, **43**, 215–225.
89 P. Pookmanee, P. Somsri, S. Phanichphant and C. Thanachayanont, *Key Eng. Mater.*, 2020, **861**, 337–343.
90 X. Zhang, Y. Yu, D. Jiang, Y. Jiao, Y. Wu, Z. Peng, J. Zhou, J. Wu and Z. Dong, *Ceram. Int.*, 2019, **45**, 6693–6701.
91 V. T. Quyen, K. Jitae, P. T. Huong, D. M. Thanh, N. M. Viet and P. Q. Thang, *Sol. Energy*, 2021, **218**, 150–156.
92 R. Ahmadiasl, G. Moussavi, S. Shekoohiyan and F. Razavian, *Catalysts*, 2022, **12**, 1310.
93 L. Liu, X. Gu, C. Sun, H. Li, Y. Deng, F. Gao and L. Dong, *Nanoscale*, 2012, **4**, 6351–6359.
94 T.-D. Pham and B.-K. Lee, *J. Catal.*, 2017, **345**, 87–95.
95 X. Zhang, C. Xu, L. Zhang, Z. Li, J. Hong and Y. Zhang, *ACS Appl. Energy Mater.*, 2022, **5**, 4564–4576.
96 J. Jang, S. Zhu, E. P. Delmo, T. Li, Q. Zhao, Y. Wang, L. Zhang, H. Huang, J. Ge and M. Shao, *EcoMat*, 2023, **5**, e12334.
97 C. Zhang, M. F. Calegari Andrade, Z. K. Goldsmith, A. S. Raman, Y. Li, P. M. Piaggi, X. Wu, R. Car and A. Selloni, *Nat. Commun.*, 2024, **15**, 10270.
98 H. Ali, R. Golnak, R. Seidel, B. Winter and J. Xiao, *ACS Appl. Nano Mater.*, 2020, **3**, 264–273.
99 P. Qiu, Y. Zhang and G. Cheng, *Int. J. Hydrogen Energy*, 2022, **47**, 10628–10637.
100 J. Minsu, N. H. Judy, S. Jason, N. Yun Hau, J. Yijiao and A. Rose, *Appl. Catal., A*, 2016, **521**, 190–201.
101 Z. Wang, Y. Liu, D. J. Martin, W. Wang, J. Tang and W. Huang, *Phys. Chem. Chem. Phys.*, 2013, **15**, 14956–14960.
102 H. Guzmán, F. Salomone, S. Bensaid, M. Castellino, N. Russo and S. Hernández, *ACS Appl. Mater. Interfaces*, 2022, **14**, 517–530.
103 F. Zhongyuan, M. Xinyi, X. Bing, H. Xiaoyun, F. Jun and L. Enzhou, *Int. J. Hydrogen Energy*, 2021, **46**, 19373–19384.
104 L. Martin, H. Martinez, D. Poinot, B. Pecquenard and F. Le Cras, *J. Phys. Chem. C*, 2013, **117**, 4421–4430.
105 M. C. Biesinger, *Surf. Interface Anal.*, 2017, **49**, 1325–1334.
106 N. Kalita, U. Nath, A. Singha, M. Sarma and M. Qureshi, *J. Mater. Chem. A*, 2025, **13**, 10723–10735.
107 H. T. Assaouka, I. N. Nsangou, D. M. Daawe, D. O. Mevoa, A. A. Zigla, P. N. Ndouka and P. M. Kouotou, *Energy Adv.*, 2023, **2**, 829–842.
108 J. Lei, S. Wang and J. Li, *Ind. Eng. Chem. Res.*, 2020, **59**, 5583–5590.
109 S. Benkoula, O. Sublemontier, M. Patanen, C. Nicolas, F. Sirotti, A. Naitabdi, F. Gaie-Levrel, E. Antonsson, D. Aureau, F.-X. Ouf, S.-I. Wada, A. Etcheberry, K. Ueda and C. Miron, *Sci. Rep.*, 2015, **5**, 15088.
110 S. Hosseinpour, F. Tang, F. Wang, R. A. Livingstone, S. J. Schlegel, T. Ohto, M. Bonn, Y. Nagata and E. H. G. Backus, *J. Phys. Chem. Lett.*, 2017, **8**, 2195–2199.
111 G. Gonella, E. H. G. Backus, Y. Nagata, D. J. Bonthuis, P. Loche, A. Schlaich, R. R. Netz, A. Kühnle, I. T. McCrum, M. T. M. Koper, M. Wolf, B. Winter, G. Meijer, R. K. Campen and M. Bonn, *Nat. Rev. Chem.*, 2021, **5**, 466–485.
112 N. Zhang, X. Feng, D. Rao, X. Deng, L. Cai, B. Qiu, R. Long, Y. Xiong, Y. Lu and Y. Chai, *Nat. Commun.*, 2020, **11**, 4066.
113 Y. Liu, X. Wu, H. Lv, Y. Cao and H. Ren, *Dalton Trans.*, 2019, **48**, 1217–1225.
114 W.-C. Peng, Y.-C. Chen, J.-L. He, S.-L. Ou, R.-H. Horng and D.-S. Wuu, *Sci. Rep.*, 2018, **8**, 9255.
115 M. Honda, T. Ochiai, P. Listiani, Y. Yamaguchi and Y. Ichikawa, *Materials*, 2023, **16**, 639.
116 H. She, Z. Zhao, W. Bai, J. Huang, L. Wang and Q. Wang, *Mater. Res. Bull.*, 2020, **124**, 110758.

117 S. Zhuxing, F. Siyuan, L. Yan and H. Yun Hang, *Chem. Eng. J.*, 2019, **375**, 121909.
118 G. Iijima, T. Inomata, H. Yamaguchi, M. Ito and H. Masuda, *ACS Catal.*, 2019, **9**, 6305–6319.
119 I. Platzman, R. Brener, H. Haick and R. Tannenbaum, *J. Phys. Chem. C*, 2008, **112**, 1101–1108.
120 W. R. Siah, H. O. Lintang, M. Shamsuddin, H. Yoshida and L. Yuliati, *Catal. Sci. Technol.*, 2016, **6**, 5079–5087.
121 J. Tang, J. R. Durrant and D. R. Klug, *J. Am. Chem. Soc.*, 2008, **130**, 13885–13891.
122 G. Vitiello, L. Clarizia, W. Abdelraheem, S. Esposito, B. Bonelli, N. Ditaranto, A. Vergara, M. Nadagouda, D. D. Dionysiou, R. Andreozzi, G. Luciani and R. Marotta, *ChemCatChem*, 2019, **11**, 4314–4326.
123 M. Asadinamin, A. Živković, N. H. de Leeuw and S. P. Lewis, *ACS Appl. Mater. Interfaces*, 2024, **16**, 35781–35792.
124 R. Greco, R. Botella and J. Fernández-Catalá, *Hydrogen*, 2023, **4**, 620–643.
125 P. Qiao, X. Wang, J. Liu, Y. Liu, M. Dai, R. Piao, Y. Liu, W. Wang, Y. Wang and H. Song, *React. Chem. Eng.*, 2023, **8**, 3028–3036.
126 L. Clarizia, G. Vitiello, R. Bericat Vadell, J. Sá, R. Marotta, I. Di Somma, R. Andreozzi and G. Luciani, *Int. J. Mol. Sci.*, 2023, **24**, 2004.
127 P. Yang, Z.-J. Zhao, X. Chang, R. Mu, S. Zha, G. Zhang and J. Gong, *Angew. Chem., Int. Ed.*, 2018, **57**, 7724–7728.

